Nanoscale

ROYAL SOCIETY OF CHEMISTRY

PAPER

View Article Online
View Journal | View Issue

Cite this: *Nanoscale*, 2023, **15**, 18716

Bimodal modulation of *in vitro* angiogenesis with photoactive polymer nanoparticles†

Gabriele Tullii, *[a] Edgar Gutierrez-Fernandez,[b] Carlotta Ronchi,[a] Christian Bellacanzone, [a] Luca Bondi,[c] Miryam Criado-Gonzalez, [b] Paola Lagonegro,[a] Francesco Moccia,[d] Tobias Cramer, [c] David Mecerreyes, [b,e] Jaime Martín [b,f] and Maria Rosa Antognazza *[a]

Angiogenesis is a fundamental process in biology, given the pivotal role played by blood vessels in providing oxygen and nutrients to tissues, thus ensuring cell survival. Moreover, it is critical in many life-threatening pathologies, like cancer and cardiovascular diseases. In this context, conventional treatments of pathological angiogenesis suffer from several limitations, including low bioavailability, limited spatial and temporal resolution, lack of specificity and possible side effects. Recently, innovative strategies have been explored to overcome these drawbacks based on the use of exogenous nano-sized materials and the treatment of the endothelial tissue with optical or electrical stimuli. Here, conjugated polymer-based nanoparticles are proposed as exogenous photo-actuators, thus combining the advantages offered by nanotechnology with those typical of optical stimulation. Light excitation can achieve high spatial and temporal resolution, while permitting minimal invasiveness. Interestingly, the possibility to either enhance (≈+30%) or reduce (up to −65%) the angiogenic capability of model endothelial cells is demonstrated, by employing different polymer beads, depending on the material type and the presence/absence of the light stimulus. *In vitro* results reported here represent a valuable proof of principle of the reliability and efficacy of the proposed approach and should be considered as a promising step towards a paradigm shift in therapeutic angiogenesis.

Received 9th June 2023,
Accepted 17th October 2023

DOI: 10.1039/d3nr02743k

rsc.li/nanoscale

1. Introduction

The manipulation of angiogenesis, *i.e.*, the endothelial cell-mediated formation of new blood vessels from the pre-existing vasculature,[1] has attracted great interest from the scientific community, since several important diseases are closely associated with an alteration of this physiological process. During the last few decades, much research effort has been put towards the development of novel therapeutic approaches targeted to both the promotion of angiogenesis, in the case of vascular damage due to cardiovascular diseases, and its inhibition for the treatment of hypervascular conditions, for example in the cases of cancer and ocular diseases.[1–3]

Currently, available treatments rely on the employment of chemically controlled methods, mainly based on angiogenesis-inducing cytokines (hepatocyte growth factor, HGF; vascular endothelial growth factor, VEGF; basic-fibroblast growth factor, bFGF;) or anti-angiogenic drug molecules (pazopanib, sunitinib, sorafenib, for example). However, these methods have several drawbacks, such as limited spatial and temporal resolution of administration, lack of reversibility, non-specificity, a short half-life, poor bioavailability, adverse side effects, hemorrhagic complications, high cost and drug resistance.[2–7]

The use of exogenous nano-sized materials has recently been proposed as a strategy to overcome some of these disadvantages and to achieve selective and reliable modulation of angiogenesis. Among other possibilities, polymeric nanoparticles have been extensively reported as passive carriers for the delivery of pro- and anti-angiogenic drugs, providing a lower risk of systemic toxicity and a higher tissue diffusion of drugs together with a better stability in blood circulation.[8,9]

Interestingly, several carbon-based and inorganic nanoparticles have also been considered as active materials, for

[a]*Center for Nano Science and Technology, Istituto Italiano di Tecnologia, Via Rubattino 81, 20134 Milano, Italy. E-mail: gabriele.tullii@iit.it, mariarosa.antognazza@iit.it*
[b]*POLYMAT, University of the Basque Country UPV/EHU, Paseo Manuel de Lardizabal 3, 20018 Donostia-San Sebastián, Spain*
[c]*DiFA University of Bologna, Viale Carlo Berti Pichat 6/2 Bologna, 40127, Italy*
[d]*Department of Biology and Biotechnology "Lazzaro Spallanzani", University of Pavia, 27100 Pavia, Italy*
[e]*Ikerbasque, Basque Foundation for Science, 48013 Bilbao, Spain*
[f]*Universidade da Coruña, Campus Industrial de Ferrol, CITENI, Campus Esteiro S/N, 15403 Ferrol, Spain*
† Electronic supplementary information (ESI) available. See DOI: **https://doi.org/10.1039/d3nr02743k**

their intrinsic pro- or anti-angiogenic properties.[7,8,10] The opportunity to employ physical stimuli recently emerged as a promising alternative to conventional methods, potentially capable of overcoming current limitations like temporal irreversibility, poor selectivity and low spatial resolution. For example, electric stimulation was demonstrated to enhance angiogenesis in skeletal muscle and endothelial cells,[11] in rabbits with myocardial infarction[12] and in human upper arm biopsy samples.[13] Jeong *et al.*[14] recently showed an enhancement in the formation of arterioles and capillaries in a mouse model of ischemia through the electrical stimulation provided with a wearable solar cell.

In this context, optically-controlled methods are particularly appealing since they offer, with respect to not only traditional chemical approaches but also electric-based methods, unsurpassed space and time resolution together with lower invasiveness. Optogenetics[15] was successfully employed for the promotion of angiogenesis *in vivo* in a mouse dorsal window chamber model[16] and for the regulation of pathologic neovascularization in mouse models for eye diseases.[17] Unfortunately, the application of this technique in human subjects is limited by the safety constraints raised from the need for viral transfer of cells and tissues with exogenous DNA.[18] Therefore, gene-less approaches have also been explored, including photobiomodulation techniques and photothermal stimulation.[19–23] In the first case, visible and NIR light excites cell chromophores (hemoglobin, myoglobin, cytochrome C oxidase, among others),[24] while in the second case heat is generated by water excitation; both processes can lead to cell membrane potential variation, non-toxic generation of nitrogen and oxygen species, and expression of pro- or anti-angiogenic genes. However, these solutions hardly provide the necessary efficacy (limited optical absorption of chromophores), dynamic range of stimulation (constraints on usable light energy density), and spatial resolution (rapid heat diffusion). Recently, we pioneered a novel approach based on the use of light-responsive semiconducting polymers. We demonstrated sizable promotion of the proliferation and formation of the tubular assembly in endothelial colony-forming cells (ECFCs), unequivocally mediated by photoexcitation of the functional material poly(3-hexylthiophene) (P3HT) in the form of thin films.[2,25–27]

However, the use of P3HT polymer thin films, while fully compatible with *in vitro* cell cultures,[28–31] represents a serious limitation for *in vivo* applications, for different reasons: (i) P3HT mainly absorbs light in the 400–600 nm spectral range, which displays a limited penetration through biological tissue;[32] (ii) thin films, though thin and fully conformable, require surgical implantation; (iii) it is necessary to extend the choice of suitable, biocompatible materials, in order to both achieve bimodal pro- or anti-angiogenesis modulation, and widen the range of suitable light densities, based on different optical absorption and charge generation efficiencies.

In the present work, we take a step forward towards all these three targets, by using, besides the prototypical P3HT as a comparison, two low band-gap conjugated polymers, commonly employed in high performance organic solar cells,[33,34] namely poly[(2,6-(4,8-bis(5-(2-ethylhexyl)thiophen-2-yl)-benzo[1,2-*b*:4,5-*b*′]dithiophene))-*alt*-(5,5-(1′,3′-di-2-thienyl-5′,7′-bis(2-ethylhexyl)benzo[1′,2′-*c*:4′,5′-*c*′]dithiophene-4,8-dione)] (PBDB-T) and poly[[4,8-bis[(2-ethylhexyl)oxy]benzo[1,2-*b*:4,5-*b*′]dithiophene-2,6-diyl][3-fluoro-2-[(2-ethylhexyl)carbonyl]thieno[3,4-*b*]thiophenediyl]] (PTB7). Both materials are characterized by a red-shifted light absorption with respect to the prototypical P3HT. We process the materials in the form of nanoparticles (NPs), thus providing the possibility to employ variable routes of not-invasive administration (including oral application and inhalation), as well as to selective cell targeting down to the subcellular length scale.[35,36] Furthermore, we demonstrate that the use of different materials combined with appropriate illumination conditions enables the modulation of pro- or anti-angiogenic responses in human umbilical vein endothelial cells (HUVECs), employed here as a valuable model for the study of the endothelium function.[37]

2. Materials and methods

2.1 Materials

Regioregular P3HT (Sigma-Aldrich) has a molecular weight (M_w) of 115–135 kDa. PTB7 was purchased from Ossila, batch M216, M_w = 78 kDa. PBDB-T was purchased from Ossila, batch M1002 (M_w = 70 kDa). Pluronic® F127 (powder, BioReagent), Phosphate-Buffered Saline (PBS) tablets, penicillin and streptomycin were purchased from Sigma-Aldrich.

2.2 Fabrication of nanoparticles by flash precipitation

The nanoparticles of conjugated polymers were prepared by flash precipitation[38,39] (or reprecipitation method), summarized in Fig. S1.† Firstly, the conjugated polymer and Pluronic® F127 were dissolved together in tetrahydrofuran (THF) at a concentration of 1 mg mL^{-1}. We initially considered three relative mass compositions between the conjugated polymer and Pluronic® (9 : 1, 3 : 1 or 1 : 1). The solutions were continuously stirred at 60 °C for one hour. Then, 1 mL of the organic solution was injected into 10 mL of PBS solution (0.01 M) under stirring at 1300 rpm. Since nanoprecipitation was almost immediately achieved, after 10 seconds the dispersion was placed in a beaker and continuously stirred at 50 °C for one hour until complete evaporation of THF. Then, the NP dispersion was dialyzed in Milli-Q water for three days, using Visking membranes (Visking DTV by Medicell Int Ltd.; cut-off range of 12–14 kg mol^{-1} with a diameter of 25.5 mm). Finally, the dispersion was centrifuged at 500 rpm for 10 minutes to separate the remaining fraction of macroscopic aggregates. The dispersion was finally stored at 4 °C under dark conditions to avoid aggregation. Prior to any *in vitro* experiment, the dispersions were lyophilized using a freeze-dryer (Telstar ®) at −83 °C and a pressure of 0.2 mbar for 48 hours. The lyophilization process allowed minimizing the presence of pathogenic agents and re-dispersing the nanoparticles directly in the cell-growth medium at an appropriate concentration of

polymer mass. Finally, the NPs were dispersed in endothelial cell medium, enriched with 100 mg mL^{-1} penicillin and 100 mg mL^{-1} streptomycin, at a concentration of 40 μg mL^{-1} under sterile conditions. This dispersion was finally diluted in the cell culture wells employed for the experiments at the chosen final concentration.

2.3 UV-vis absorption

Light absorption measurements were performed with a Shimadzu UV-2550 spectrophotometer. The samples were prepared by pouring the dispersion into disposable cuvettes. The range of measurement was set between 400 and 900 nm.

2.4 Dynamic light scattering (DLS)

DLS and zeta-potential measurements were performed with a Malvern Zetasizer Nano SZ. Samples were prepared by pouring the dispersion into disposable folded cuvettes in the case of DLS and into DTS1070 cells for zeta-potential measurement.

2.5 Transmission electronic microscopy (TEM)

TEM measurements were performed on a TECNAI G2 20 TWIN operated at 200 kV and equipped with a LaB_6 filament. Samples were prepared by casting a droplet of the dispersion onto a copper TEM grid (300 Mesh) covered by a pure carbon film and dried at ambient temperature. The grid was glow-discharged before putting the drop of suspension.

2.6 Nanoparticles' photocurrent spectroscopy

Monochromatic light was generated with a xenon light source (250 W) and a Cornerstone 260 monochromator (entrance slit 2 mm, exit slit 2 mm). A rotating disc chopper was used to modulate the light at 7 Hz. For measurements with wavelengths greater than 400 nm, a 400 nm longpass filter was inserted into the beam to avoid second harmonics. The measurement cell was positioned at 70 mm from the monochromator exit slit. At that position, an average light intensity of 219 ± 8 μW cm^{-2} was measured in the range between 400 and 800 nm. The measurement cell was made of aluminum and had a PDMS liquid reservoir containing the nanoparticle suspension (*ca.* 200 μL). The suspension was illuminated through a glass window and was in contact with an ITO-covered glass slide, used as the working electrode. An Ag|AgCl wire served as a quasi-reference/counter electrode. The grounded aluminum structure acted also as a Faraday cage. Multiple reflections and ambient light were carefully screened. The detection of the photocurrent signal, as well as the control of the potential applied to the working electrode, was accomplished by using a lock-in amplifier (ZHINST, MFLI), set at the chopping frequency. Spectra have been properly normalized by taking into account the detector spectral responsivity, the emission spectrum of the light source and the spectral efficiency curves of the gratings of the monochromator.

2.7 Cell culture of HUVECs

The HUVEC line was purchased from PromoCell. The cells were grown on culture flasks coated with 0.2% gelatin in endothelial cell medium (endothelial cell basal medium 2, PromoCell), enriched with an endothelial cell GM 2 supplement pack (PromoCell), and maintained at 37 °C, 5% CO_2. For the experiments, only HUVECs at passage <7 were employed. For all experiments, HUVECs were plated on glass slides at 7×10^3 cells per cm^2 density and after 3 h from plating, the cells were incubated with the different NPs at 20 μg mL^{-1} concentration for 20 h. The NP-treated samples were rinsed with Krebs Ringer's (KRH) extracellular solution to remove non-internalized NPs at the beginning of each measurement. HUVECs plated on glass slides without NPs were used as a control (CTRL).

2.8 AlamarBlue viability assay

HUVECs were plated in 12-well plates by employing cell growth medium without phenol red. Cell proliferation was evaluated 24, 48, and 120 h after incubation. Prior to measurements at each time point, the growth medium was replaced with fresh medium containing 100 mg mL^{-1} alamarBlue (Thermo Fisher). The alamarBlue reagent is based on resazurin, a cell-permeable non-fluorescent compound that upon entering living cells is reduced to a highly fluorescent resorufin. The fluorescence of the latter is thus an indicator of the viability and proliferation of cells. The samples were incubated for 3 h at 37 °C, 5% CO_2 in the dark. Then, three aliquots of culture media (100 μL) were placed in black 96-well microplates and their fluorescence was acquired using a Tecan Spark microplate reader (excitation wavelength: 530 nm, emission acquired at 590 nm).

2.9 Confocal imaging

Cell membrane and nuclei were stained, respectively, with Cell Mask Green (Thermo Fisher; exc/em wavelength, 522/535 nm) and Hoechst (Thermo Fisher; exc/em, 350/461 nm). *Z*-Stacks were acquired with an upright microscope (Olympus BX63), equipped with a 60× water immersion objective, a spinning disk confocal module (X-Light V2 spinning disk module from Crest Optics), and an sCMOS camera (Prime BSI, Teledyne Photometrics; Tucson, Arizona, USA). The system, comprising LED and laser light sources (Spectra III and Celesta, from Lumencor), was assembled by Crisel Instruments. Excitation/emission wavelengths were 530/660 nm for P3HT NPs and 636/690 nm for PTB7 and PBDB-T NPs. The experiments were carried out at room temperature, by employing a KRH extracellular solution (mM): 135 NaCl, 5.4 KCl, 1.8 $CaCl_2$, 1 $MgCl_2$, 5 HEPES, 10 glucose, pH adjusted to 7.4 with NaOH. Images were processed with ImageJ.

2.10 *In vitro* angiogenesis assay

HUVECs were cultured and treated with NPs as described in section 2.7. After 20 h of incubation with NPs, the cells were detached, resuspended and plated on 96-well plates pre-treated with 90 μL of Geltrex LDEV-Free Reduced Growth Factor Basement Membrane Matrix (Thermo Fisher) at 4×10^4 cells per cm^2. The plates were maintained at 37 °C, 5% CO_2 and optically excited with LED light sources (central excitation

wavelength: 660 nm, 6 mW cm^{-2}) or left in the dark. The capillary network formation was assessed 6 h later by acquiring bright-field images with an inverted microscope (Nikon Eclipse Ti). The quantification of the main features of the capillary-like network was performed by employing the Angiogenesis Analyzer plug-in of ImageJ.[40] Mean values were averaged over 12 fields of view belonging to 3 independent experimental sessions.

2.11 Intracellular reactive oxygen species (ROS) detection

2′,7′-Dichlorodihydrofluorescein diacetate (H_2DCF-DA, purchased from Sigma Aldrich) was employed for intracellular detection of ROS. NP-treated cells and control, untreated cells were photo-excited by illuminating each sample for 3 min with an LED system (Lumencor Spectra X light engine, λ = 660 nm, 37 mW mm^{-2}) fiber-coupled to an inverted microscope (Nikon Eclipse Ti). Subsequently, cells were incubated with H_2DCF-DA for 30 min in KRH (10 μM). After careful wash-out of the excess probe from the extracellular medium, the fluorescence of the probes was recorded (exc/em 490/520 nm; integration time, 50 ms; binning: 1 × 1) with an inverted microscope (Nikon Eclipse Ti) equipped with a 20× objective and an sCMOS camera (Prime BSI, Teledyne Photometrics; Tucson, Arizona, USA). Variation of the fluorescence intensity was evaluated over the regions of interest covering single-cell areas. Reported values represent the average over multiple cells (n > 40) belonging to 2 statistically independent samples. Image processing was carried out with ImageJ. Origin Pro 2018 was employed for data analysis.

2.12 Ca^{2+} imaging experiments

The experiments were carried out at room temperature, by employing KRH extracellular solution and the same microscope used for confocal imaging experiments. HUVECs were incubated with 1.5 μM Ca^{2+} sensitive dye FLUO4-AM (Thermo Fisher; exc/em 488/515 nm) for 20 min and washed out for 10 min. The fluorescence of the FLUO4AM probe was acquired for 3 minutes (an LED coupled to an upright microscope (Olympus BW63), 20× objective; spectral emission peaked at 474 nm, 5 mW mm^{-2}) while the simultaneous photoexcitation of the NPs was performed with a laser diode, emission peak at 660 nm, coupled to an upright microscope (Olympus BW63, 20× objective, 12 or 37 mW mm^{-2}). Variation of the fluorescence intensity was evaluated over the regions of interest covering single-cell areas. Evaluated features of intracellular Ca^{2+} dynamics comprise the peak amplitude (PA) normalized to the baseline fluorescence F_0, the rise slope (Ca^{2+} rise) and the decay slope (Ca^{2+} decay).

3. Results and discussion

3.1 Conjugated polymer nanoparticles (NPs) fabrication and characterization

The polymer nanoparticle (NP) dispersions are prepared by the flash nanoprecipitation method (Fig. S1†). In order to enhance the stability of the suspension in the ionic medium, an amphiphilic triblock copolymer surfactant, Pluronic® F127, is added in the process.[41] Pluronic® block copolymers have been widely used to enhance the biocompatibility, water solubility and stability of drug delivery systems, upconversion NPs and innovative nanocarriers.[42,43] In particular, Pluronic® F127 was successfully employed for the fabrication of stable water dispersions of carbon nanomaterials[44] and conjugated polymer NPs,[41,45] including PTB7 NPs.[46]

Fig. 1a shows the chemical structures of the three conjugated polymers employed in this work (P3HT, PTB7 and PBDB-T), as well as the photographs of the dispersions obtained at three polymer : Pluronic® relative concentrations, showing good optical transparency in all cases. UV-vis absorption spectra of P3HT, PTB7 and PBDB-T NP dispersions are depicted in Fig. 1b. P3HT NPs show a maximum absorption at 550 nm and the characteristic vibronic peaks at approximately 520, 550 and 610 nm, similar to what seen in the case of P3HT thin films.[47] The absorption spectra of PTB7 and PBDB-T NPs show the main absorption peaks at 620/580 nm and secondary vibronic peaks at 690/630–650 nm, respectively. Interestingly, all the fabricated NPs absorb stronger at the lower-energy vibronic peak. We attribute this finding to a high degree of crystallinity in the case of P3HT[48] and to more pronounced interchain interactions and better-ordered packing in PBDB-T and PTB7.[46,49,50] This aggregation effect is directly related to the presence of sodium chloride ions during the NP nucleation and growth process. In contrast, when the fabrication of polymer : Pluronic® NPs is done in pure water, a significant decrease in the lower-energy vibronic peak absorption is observed (Fig. S2†). In addition, PTB7 and PBDB-T NPs fabricated in saline PBS solution show red-shifted absorption spectra when compared to the NPs fabricated in pure water. The PBS-induced effects are reduced in the case of the highest

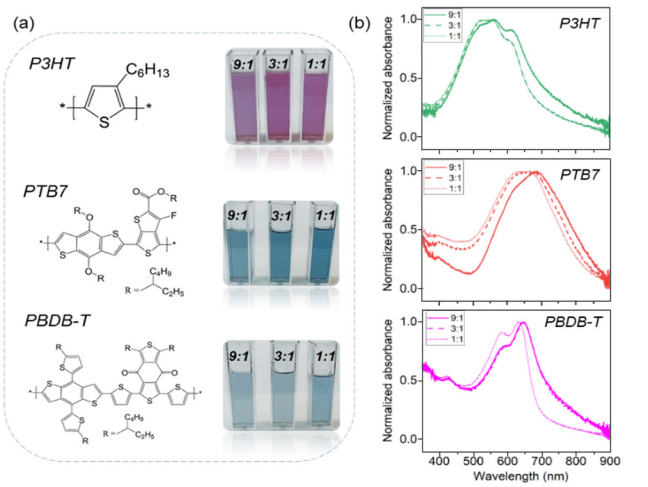

Fig. 1 (a) Chemical structures of the commercial conjugated polymers used in this work and photographs of the corresponding polymeric colloids obtained, at three polymer : Pluronic® F127 relative concentrations. (b) UV-vis absorption spectra of NP aqueous dispersions.

content of Pluronic® (1 : 1 mass relation with the polymers), possibly as a consequence of the shield that the surfactant molecules establish between the conjugated polymer chains and the ionic species of PBS during the nanoparticle formation (Fig. 1b). A similar aggregation effect was observed in P3HT NP formation by using different surfactants.[51]

The size and shape of the nanoparticles were characterized by TEM and DLS (Fig. 2, Fig. S3 and Table S1†). TEM images display spherical-shaped NPs and size-distribution values within the range of 100–200 nm. The diameters measured by DLS are systematically larger than those found by TEM, with the size distribution centered at around 250–300 nm. This difference is observed at all Pluronic® concentrations (Table S1 and Fig. S3†), and it can be explained by the contribution of the hydrodynamic diameter and the Pluronic® corona swelling around the polymeric NP core in DLS measurements only. The highest concentration of Pluronic® employed (1 : 1 polymer : Pluronic® mass ratio) induces the formation of surfactant micelles and less regular nanoparticles (Fig. S3†).

Pluronic® F127 is a non-ionic surfactant, so it increases the colloidal stability due to the steric, non-ionic repulsion between the shells around NPs. The zeta-potential values at different time points confirm optimal colloidal stability, even in the case of a lower Pluronic® concentration (*i.e.*, 9 : 1 relative mass concentration), up to 10 days post-fabrication. *Z*-Potential values are below −20 mV in all considered materials (Table 1). Therefore, we opted for the 9 : 1 formulation in all the following experiments.

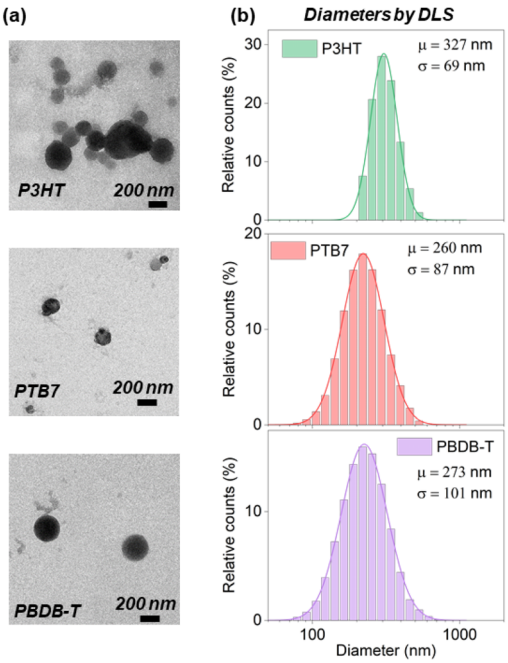

Fig. 2 (a) TEM images of P3HT, PTB7 and PBDB-T NPs with 9 : 1 polymer : Pluronic® relative mass concentration. (b) Size distribution obtained by DLS: μ and σ correspond to the mean and the standard deviation, respectively.

Table 1 Zeta-potential values of conjugated polymer NPs at a relative mass concentration of 9 : 1 (polymer : Pluronic®)

Zeta potential (mV)		
	As prepared	After 10 days
P3HT	−29.7 ± 0.3	−31.9 ± 0.8
PTB7	−35.4 ± 0.9	−35.7 ± 0.5
PBDB-T	−26.0 ± 1.3	−21.9 ± 0.4

3.2 Photoelectrochemical current spectroscopy

In our previous work, we reported P3HT-based NPs' photoelectrochemical activity, and we showed that they maintain the capability to generate charges and to work in a photocathodic mode in an oxygenated aqueous environment.[52] The photoelectrochemical activity of the NPs generates Reactive Oxygen Species (ROS), which are known to play a pivotal signaling role both in pro-angiogenesis and anti-angiogenesis processes. However, in a previous study, NPs were realized without any surfactant. Conversely, in the present work Pluronic® 127 was used to guarantee suitable colloidal stability over a longer term, good biocompatibility and optimal repeatability in the fabrication process for all the considered conjugated polymers. Thus, it is necessary to assess whether Pluronic®-coated NPs preserve their photoelectrochemical activity towards oxygen reduction.

Fig. 3 shows the photoelectrochemical current spectra for P3HT, PTB7 and PBDB-T NPs, at a 9 : 1 polymer : Pluronic® relative mass concentration. The photocurrent spectra are very similar to the optical absorption spectra as a typical feature of a symbatic-like behavior. Accordingly, absorbed photons contribute equally to the photocurrent generation, independently of their energy. We hence exclude a significant contribution of defect states or interfacial energy levels to the process. Instead, the photoelectrochemical activity relies on bulk optical bandgap absorption leading to exciton formation, thermalization and subsequent dissociation into free charge carriers in the NPs. Free electronic carriers participate in the electrochemical reduction of oxygen in the solution leading to ROS formation. Here, the process gives rise to a macroscopic cathodic current at the working electrode, with the occurrence of electron transfer and oxygen reduction processes. The amplitude of the current is correlated with the different properties of NP dispersions, such as the amount of NPs in solution, the quantum efficiency of the photoelectrochemical process and the charge storage capability of the NPs.

The findings are in line with previous results obtained with P3HT NPs and demonstrate the occurrence of photo-electrochemical reactions at the polymer/buffer interface of NPs, mostly leading to oxygen reduction processes and the formation of ROS species, all virtually ending up in hydrogen peroxide formation at timescales >1 s. In biological tissue, intracellular and extracellular H_2O_2 concentrations represent a powerful signaling event for the modulation of angiogenic processes. The possibility to modulate it on demand and over

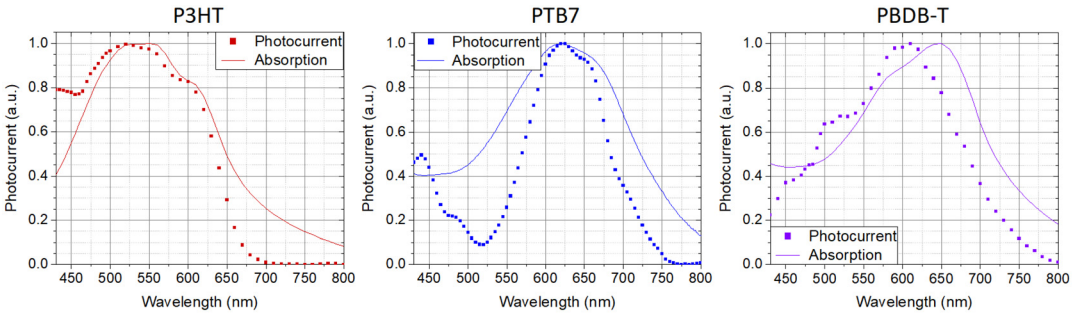

Fig. 3 Comparison between NPs' absorption spectra and corresponding photoelectrochemical current spectra.

different orders of magnitude, through contactless optical excitation of smart nanomaterials, may open a path to interesting therapeutic applications. Thus, we next investigate the coupling between polymer NPs and endothelial cells.

3.3 Conjugated polymer NPs' biocompatibility and internalization within living cells

We select Human Umbilical Vein Endothelial Cells (HUVECs) as a valuable model, largely accepted in the literature for the study of the main biological pathways involved in endothelium function, including normal and neoplastic proliferation, migration and angiogenesis, as well as for the development of therapies against cancer and cardiovascular diseases.[37,53]

The viability and proliferation of HUVECs treated with NPs are assessed by the alamarBlue assay at three different time points (Fig. 4a). Different NP concentrations are preliminarily investigated, in the range of 10–50 μg mL^{-1}; detrimental effects on cell viability are observed only in the case of 50 μg mL^{-1}, with reduced proliferation (data not shown). By adopting a conservative approach, the concentration is then fixed at 20 μg mL^{-1}. Data show that the cell metabolic activity is preserved in the presence of all considered NPs, up to 120 hours after plating. Interestingly, one can notice a higher proliferation increase, in percentage, between 24 and 120 hours after plating in the case of HUVECs treated with NPs (+226% for P3HT, +187% for PBDB-T and +384% for PTB7) in comparison to the untreated ones (CTRL, +169%). Moreover, we investigated the capability of NPs to internalize within the intracellular environment, by means of confocal microscopy (Fig. 4b–d). The most critical parameters governing the capability of NPs to cross the plasma membrane and to internalize within the cell cytosol are the shape, the size and the *z*-potential. TEM, DLS and *z*-potential measurements (Fig. 2 and Table 1) demonstrated that there are no appreciable differences among the three considered NPs. Based on these data, no sizable difference in the internalization process is expected. Moreover, all considered materials comprise the same surfactant (Pluronic® F127) with the same relative concentration (9 : 1, polymer : Pluronic®). Thus, also the chemical–physical interaction with cell proteins is expected to be similar. In order to clarify this hypothesis, confocal images are acquired at different *z* planes from the cell upper surface to the bottom

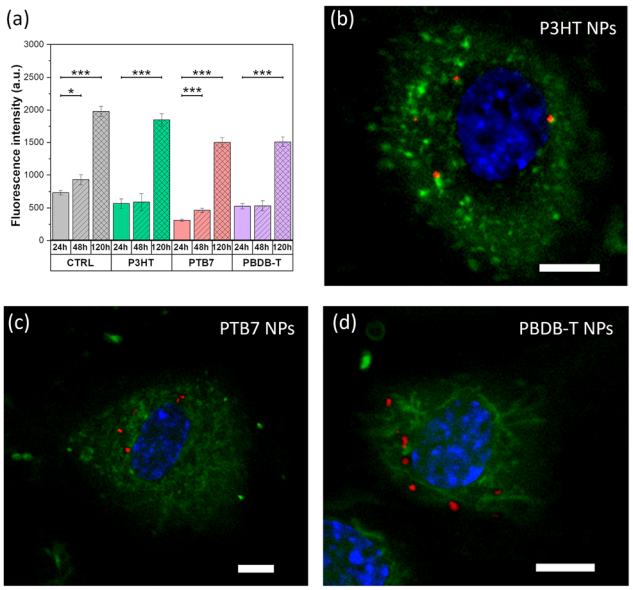

Fig. 4 (a) Viability of HUVECs, incubated with the different NPs, evaluated as the fluorescence of the reduced form of the alamarblue cell-viability reagent. Data were compared using the nonparametric Mann–Whitney *U*-test (0.05 significance level). **p* < 0.05, ****p* < 0.001. Error bars represent the standard error of the mean (sem). Representative confocal images depicting HUVECs loaded with P3HT (b), PTB7 (c) and PBDB-T (d) NPs acquired at a *z* plane corresponding to the cell inner part. Cells are stained with Cell Mask Green (membrane, green) and Hoechst 33342 (nuclei, blue); NP fluorescence emission is in red. Scale bars, 5 μm.

interface (Fig. S4 and Videos S1 and S2†). Images recorded at a focal plane corresponding to the cell half height, in the middle of the cell volume, clearly show that all the three NP types (red) are successfully internalized within the cell membrane (green), however without crossing the nuclear membrane (blue, Fig. 4b–d). In addition, the 3D reconstruction of the cells provides evidence of the cell membrane integrity after the NP internalization process (Fig. S5†).

3.4 *In vitro* angiogenesis assay

We examine the physiological outcome of the red light-absorbing NPs by carrying out a tube formation assay that recapitulates many steps of the angiogenic process, including

migration, adhesion, and tubule development.[26] For this purpose, we plate NP-treated HUVECs on a widely used reconstituted basement membrane extracellular matrix, which resembles the membrane that surrounds blood vessels *in vivo* and allows cells to assemble into a bi-dimensional capillary-like network. We then expose cells to optical excitation (peak excitation wavelength, 660 nm; photoexcitation density, 6 mW cm^{-2}; 6 hours) or we leave the control samples in the dark for 6 h. The morphology of the network is studied through the analysis of bright-field images (Fig. S6† and Fig. 5). The qualitative observation of the images (Fig. S6†) denotes a tendency of HUVECs incubated with PTB7 NPs, in the dark, to organize into an extended capillary-like network formation, as compared to cells not incubated with NPs (CTRL dark, Fig. S6†). This effect is not present in the PBDB-T case, showing a comparable situation to the CTRL dark case. The system subjected to the sole red light excitation (CTRL light) does not show remarkable differences from the CTRL dark case (Fig. S6†). Conversely, when optical stimulation is coupled with PTB7 or PBDB-T NPs, the network development is reduced, as compared to the corresponding NP-treated cases in the dark (Fig. S6†). In order to confirm the qualitative observations, we performed a quantitative analysis by focusing our attention on 3 main features of the capillary-like network (Fig. 5a), namely: (1) the number of master segments, *i.e.* tubes that are connected to the rest of the network from both sides (yellow segments); (2) the number of master junctions, *i.e.* a junction that links at least three master segments (pink circles); (3) the number of meshes, *i.e.* closed areas delimited by master segments and associated master junctions (cyan loops).[26,40]

Interestingly, under dark conditions, a sizable pro-angiogenic effect is observed in the case of treatment with PTB7 NPs and is absent in the case of PBDB-T NPs. PTB7 NPs lead to a significant increase, compared to the CTRL dark conditions, in all considered features, namely in the number of master junctions (Fig. 5b), master segments (Fig. 5c) and meshes (Fig. 5d), with an increment percentage of about +33%, +37% and +31%, respectively.

Untreated, illuminated samples do not show a sizable, statistically significant variation in the tubule formation, as compared to control dark samples, thus confirming that photo-biomodulation processes have a limited or negligible effect at the considered light power density.

Conversely, optical excitation in the presence of either NP type produces a statistically relevant decrease in the number of all the 3 main features of the capillary-like network in comparison to the NP-treated HUVECs in the dark (Fig. 5b–d). Illuminated PBDB-T NPs show the more prominent anti-angiogenic effect, with the number of the master junction, master segments and meshes being about −46%, −55% and −65% lower in comparison to the NP-treated dark controls, respectively (Fig. 5b–d). In the PTB7 case, the red light-induced reduction is about −30% for all the features (Fig. 5b–d), sufficient to compensate for the pro-angiogenic effect observed in this case for samples in the dark, with the final values comparable to the untreated controls.

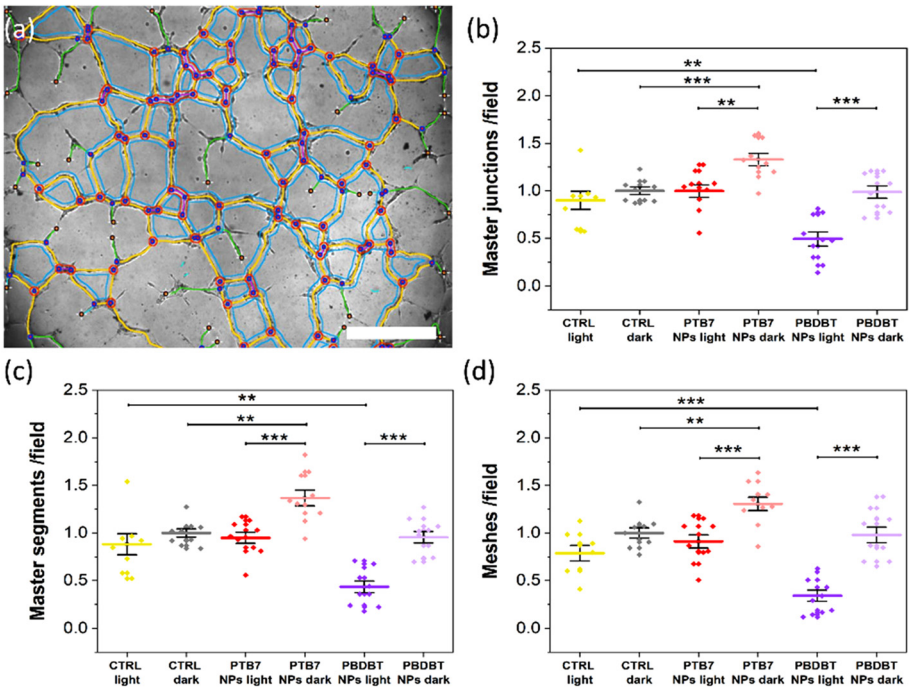

Fig. 5 (a) Representative graphical representation of the detected and vectorized components of the HUVEC capillary-like network, superimposed to the correspondent bright field image. Scale bar: 500 μm. Quantitative analysis, reporting the average number of master junctions (b), master segments (c), and meshes (d) obtained under the different conditions, 6 h from plating on the reconstituted basement membrane extracellular matrix. The results are represented as the mean ± sem of three different experiments. Data were compared with Student's *t*-test. $^{**}p < 0.01$, $^{***}p < 0.001$.

In summary, we observe two complementary interesting phenomena: a pro-angiogenic effect provided by PTB7 NPs, in the dark and a light-induced anti-angiogenic effect provided by both NPs, but much more pronounced in the case of PBDB-T NPs. The understanding of the mechanisms behind the pro- and anti-angiogenic effects observed is not straightforward, given the fact that the tube formation is an intricate process as it involves different parameters, like the proliferation and migration of endothelial cells.[1] Regarding the case of nano-sized materials, the complexity of predicting and controlling the angiogenic properties of the systems has been highlighted by different studies in recent literature.[8] Several NP types have been proposed for therapeutic angiogenesis, both inorganic/metal and carbon based, including terbium hydroxide nanorods, europium hydroxide nanorods, zinc oxide nanoflowers, silver NPs, gold NPs, copper NPs, reduced graphene oxide, graphene oxide and carbon nanotubes.[7,8] It has been demonstrated that these systems can exhibit either a pro-angiogenic or anti-angiogenic behavior depending on various parameters, including the type of material, surface properties (*e.g.* charge, wettability), size, and effective concentration.[8,54] The multiple variables involved, and their possible interlocking, make the establishment of general rules for the control of the angiogenic outcome extremely hard.[8] However, in most cases the NP properties are shown to be crucial for the intracellular ROS production, which has been reported to be one of the predominant effects that drive the angiogenic properties of nanomaterials, through the activation of specific signaling pathways.[7,8,55] Importantly, we recently demonstrated that optical excitation of P3HT thin films determines an enhancement in ECFC tubulogenesis, driven by the extracellular ROS production and activation of plasma membrane TRPV1 channels.[26] In addition, ROS have long been known to exert either a pro- or anti-angiogenic effect depending on their concentration in vascular endothelial cells.[56] In light of these reports, we assess the effects of PTB7 and PBDB-T NPs' photoexcitation on the intracellular ROS production in HUVECs.

3.5 Intracellular ROS production

Along with angiogenesis, ROS are widely involved in several physiological and pathophysiological processes.[57] Although ROS overproduction can be highly detrimental, causing oxidative stress[58] and leading in some cases to irreversible cell damage and apoptosis,[59] endogenously produced ROS are involved in different essential biological functions,[60] like immune system control,[61] metabolism regulation,[62] neurotransmission[63] and blood pressure modulation.[64] Several pathological conditions are related to the alteration in physiological ROS production, guiding the research towards innovative therapeutic systems based on ROS-responsive drug delivery systems for the controlled release of ROS.[57,65]

In order to assess the capability of the different NP systems to effectively induce intracellular ROS production, either in the dark or upon photoexcitation, we employ an intracellular ROS fluorescent probe sensitive to a large variety of different ROS (including H_2O_2, $HO^{\bullet}$, $ROO^{\bullet}$), namely 2,7-dichlorodihydrofluorescein diacetate (H_2DCF-DA).[66] This probe is hydrolysed within the intracellular environment, and the subsequent oxidation by ROS leads to the fluorescent compound 2,7-dichlorofluorescein (DCF).

Fig. 6 depicts the DCF fluorescence intensity (ΔF) recorded from HUVECs untreated (CTRL) and treated with PTB7 and PBDB-T NPs, both in the dark and under photoexcitation. The results obtained show that HUVECs treated with the two NP types PBDB-T and PTB7 NPs, in the absence of optical excitation, exhibit a comparable relative fluorescence difference (*i.e.*, intracellular ROS concentration) with respect to the untreated cells (CTRL dark). Conversely, upon light excitation (660 nm, 3 min, 37 mW mm^{-2}), HUVECs solely exposed to light (CTRL light), PTB7 and PBDB-T NP-treated ones present an increase in the DCF fluorescence of about 108%, 400% and 1500% with respect to the CTRL dark case, respectively.

Given their pivotal role in the angiogenesis process,[7,8,55] the contribution of both endogenous and exogenous ROS has been extensively investigated.[3,67] In more detail, it has been shown that NPs can induce endogenous ROS by several intracellular processes, including the impairment of the electron transport chain, the depolarization of the mitochondrial membrane and the activation of the nicotinamide adenine dinucleotide phosphate (NADPH)-like enzyme systems.[55]

ROS can be produced by different stimuli, like hypoxia and ischemia, as well as through VEGF[3,68] and they activate NADPH oxidase, which is particularly relevant for endothelial cells. In addition, NPs, in particular metal-based ones, have been reported to chemically produce exogenous ROS as well.[55] Fig. 6 shows that neither PTB7 nor PBDB-T NPs lead to an intrinsic ROS intracellular production, when not exposed to photoexcitation. This result suggests that the pro angiogenic effect observed with PTB7 NPs in the dark (Fig. 5b–d) is due to a ROS-independent mechanism. A possible explanation could be related to a change in the intracellular redox balance, as

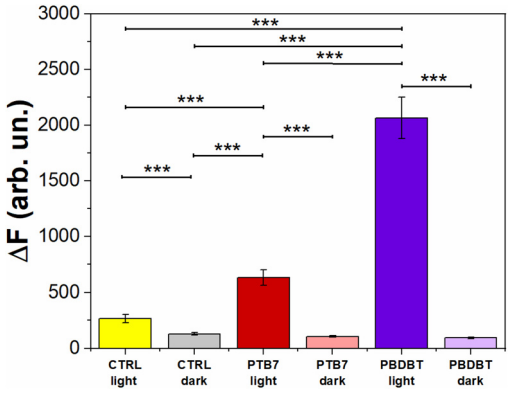

Fig. 6 Evaluation of intracellular ROS production by the measurement of the ROS-sensitive fluorophore H_2DCF-DA fluorescence intensity (ΔF) in the presence and absence (CTRL) of the different NPs under light and dark conditions. DCF probe excitation/emission wavelengths: 488/515 nm. Data were compared using the nonparametric Mann–Whitney *U*-test (0.05 significance level). $*p < 0.05$, $***p < 0.001$. Error bars represent the standard error of the mean (sem).

recently demonstrated in the case of P3HT NPs in the absence of photoexcitation.[69] The mechanisms leading to HUVECs' network enhancement deserve however in-depth investigation and will be the objective of a future dedicated work. Conversely, upon photo-stimulation, we observe a significant increase in the intracellular ROS concentration, possibly related to the observed light-induced inhibition of the capillary-like structures (Fig. 5). Noticeably, the better performing ROS-generating system, *i.e.*, PBDB-T NPs, corresponds to the most pronounced inhibition effect. This result suggests the presence of direct proportionality between the light-induced anti-angiogenic effect and the intracellular ROS concentration, in analogy with literature reports on carbon-based and inorganic NPs.[7,55,70]

Interestingly, in NP-untreated samples, we observe a red light-induced intracellular ROS increase (Fig. 6) that does not correspond to a significant variation in the HUVECs' tube formation (Fig. 5). This demonstrates that the intrinsic photostimulation of endogenous chromophores, while enough to induce ROS generation, may require higher photoexcitation densities and more aggressive stimulation protocols for achieving effective angiogenesis modulation, thus limiting the dynamic range of conditions potentially suitable for *in vivo* applications and motivating the need for the development of efficient, non-toxic, and exogenous materials. Non-toxic ROS photogeneration may also correlate with the modulation of intracellular Ca^{2+}, as observed in circulating ECFCs upon photoexcitation.[25,26] Fig. S7a† shows the representative Ca^{2+} dynamics recorded in HUVECs treated with PBDB-T and PTB7 NPs and in control, untreated samples, upon red-light photoexcitation. To achieve this goal, we used the Ca^{2+} sensitive fluorescent dye FLUO4-AM, whose absorption and emission spectra ideally have negligible overlap with the optical properties of red-light absorbing NPs. The sole exposure to red light reduces the peak amplitude (PA) in a power density-dependent manner, as evidenced in the NP-untreated HUVECs case (Fig. S7a and S7b†). In previous studies, it has been shown that red light has a direct effect on HUVEC metabolism; in particular, an enhancement in viability, proliferation and nitric oxide (NO) secretion was observed.[22,71,72] In order to study the intrinsic photothermal effect in the absence of NPs, we measure the light-induced local heating of the extracellular solution without NPs, through the calibrated pipette resistance method (Fig. S8†).[73] We found no heating of the bath at the maximum light power density employed (37 mW mm^{-2}), safely excluding the contribution of photothermal stimulation without NPs. However, the in-depth understanding of the red light-induced reduction mechanism of the Ca^{2+} PA in HUVECs deserves further investigation and additional experiments, which are not in line with the scope of the present work. Most interestingly, in this work, NP treatment and photoexcitation synergistically allow us to partially or completely counterbalance the PA decrease induced by photoexcitation only (Fig. S7b and S7c†). This effect is light-density dependent, and it is more pronounced in the case of the most efficient PBDB-T NPs, where the PA value is fully restored to its unperturbed value (Fig. S7c†). Upon optical stimulation at the lower excitation density (12 mW mm^{-2}), the PA reduction amounts at −17.3% in the CTRL group, −37% in the PTB7 group and −9% in the PBDB-T group. In contrast, the optical stimulation of the NPs at the higher excitation density (37 mW mm^{-2}), the same employed in ROS experiments (Fig. 6), strongly reduces the inhibitory light-induced effect. Even, the PA is slightly enhanced (+5%) by the photostimulation in HUVECs loaded with PBDB-T NPs, as compared to a reduction of −30% in the CTRL group (Fig. S7c†). These results show that polymer NPs can efficiently modulate the Ca^{2+} dynamics in HUVECs upon visible light excitation, suggesting a modulation of channel repertoire involved in Ca^{2+} homeostasis (*e.g.*, TRP channels).[25]

4. Conclusion

In this work, we successfully realize stable NP dispersions, based on prototypical P3HT, PBDB-T and PTB7 conjugated polymers. We focus our attention on the latter two, given their optical absorption in the red region of the visible light spectrum, favorable in view of *in vivo* applications. PBDB-T and PTB7 NPs are successfully internalized within the cytosol of HUVECs, a valuable model of endothelial function, without hampering their proliferation. Interestingly, we report that the realized NPs can have a bimodal effect on angiogenic response, either pro-angiogenic and anti-angiogenic depending on illumination conditions. In particular, PTB7 NPs sizably promote the formation of HUVECs' capillary-like network, under dark conditions, while the effect is reduced by light excitation. PBDB-T NPs instead do not have any effect under dark conditions but exhibit a pronounced anti-angiogenic outcome upon red-light excitation. Interestingly, we observe that the illumination of both PBDB-T and PTB7 NPs modulates intracellular ROS production and calcium (Ca^{2+}) dynamics, suggesting a close interplay between ROS, Ca^{2+} fluxes and the light-induced inhibition of the HUVEC tubule formation in the presence of NPs.

In conclusion, our work may open the way to novel therapeutic angiogenesis strategies *in vivo*, characterized by the possibility to achieve a bimodal control of the capillary network formation, depending on the nature of the materials and the photostimulation protocols.

Author contributions

G. Tullii: investigation, conceptualization, validation, formal analysis, and writing – original draft. E. Gutierrez-Fernandez: investigation, formal analysis, and writing – review & editing. C. Ronchi: investigation, conceptualization, validation, formal analysis, and writing – review & editing. C. Bellacanzone: investigation, formal analysis, and writing – review & editing. L. Bondi: investigation, formal analysis, and writing – review & editing. M. Criado-Gonzalez: investigation and writing – review & editing. P. Lagonegro:

formal analysis. F. Moccia: conceptualization and writing – review & editing. T. Cramer: conceptualization and writing – review & editing. D. Mecerreyes: conceptualization and writing – review & editing. J. Martín: conceptualization and writing – review & editing. M. R. Antognazza: project administration, supervision, conceptualization, and writing – original draft.

Conflicts of interest

There are no conflicts to declare.

Acknowledgements

The financial support from the EU Horizon 2020 FETOPEN-2018-2020 Programme "LION-HEARTED", grant agreement no. 828984 is acknowledged. MRA acknowledges the support from the European Research Council (ERC) under the European Union's Horizon 2020 research and innovation program 'LINCE', grant agreement no. 803621. The authors acknowledge the technical and human support provided by SGIker (UPV/EHU/ERDF, EU). Part of the fluorescence images analysis was carried out at the ALEMBIC laboratory in IRCCS Ospedale San Raffaele and Università Vita-Salute San Raffaele.

References

1 P. Carmeliet, *Nature*, 2005, **438**, 932–936.
2 F. Moccia, M. R. Antognazza and F. Lodola, *Front. Physiol.*, 2021, **11**, 616189.
3 R. Augustine, P. Prasad and I. M. N. Khalaf, *Mater. Sci. Eng., C*, 2019, **97**, 994–1008.
4 F. Elice and F. Rodeghiero, *Thromb. Res.*, 2012, **129**, S50–S53.
5 A. M. E. Abdalla, L. Xiao, M. W. Ullah, M. Yu, C. Ouyang and G. Yang, *Theranostics*, 2018, **8**, 533–548.
6 G. Dragneva, P. Korpisalo and S. Ylä-Herttuala, *Dis. Models Mech.*, 2013, **6**, 312–322.
7 A. K. Barui, S. K. Nethi, S. Haque, P. Basuthakur and C. R. Patra, *ACS Appl. Bio Mater.*, 2019, **2**, 5492–5511.
8 S. Kargozar, F. Baino, S. Hamzehlou, M. R. Hamblin and M. Mozafari, *Chem. Soc. Rev.*, 2020, **49**, 5008–5057.
9 C. Yang, H. H. Hwang, S. Jeong, D. Seo, Y. Jeong, D. Y. Lee and K. Lee, *Int. J. Nanomed.*, 2018, **13**, 6517–6530.
10 J. M. Yong, L. Fu, F. Tang, P. Yu, R. P. Kuchel, J. M. Whitelock and M. S. Lord, *ACS Biomater. Sci. Eng.*, 2022, **8**, 512–525.
11 M. Zhao, in *The Cell Cycle in the Central Nervous System*, ed. D. Janigro, Humana Press, Totowa, NJ, 2006, pp. 495–509.
12 P. Zhang, Z.-T. Liu, G.-X. He, J.-P. Liu and J. Feng, *Cell Biochem. Biophys.*, 2011, **59**, 19–27.
13 A. Sebastian, F. Syed, D. Perry, V. Balamurugan, J. Colthurst, I. H. Chaudhry and A. Bayat, *Wound Repair Regen.*, 2011, **19**, 693–708.
14 G.-J. Jeong, J. Y. Oh, Y.-J. Kim, S. H. Bhang, H.-K. Jang, J. Han, J.-K. Yoon, S.-M. Kwon, T. I. Lee and B.-S. Kim, *ACS Appl. Mater. Interfaces*, 2017, **9**, 38344–38355.
15 K. Deisseroth, *Nat. Methods*, 2011, **8**, 26–29.
16 L. R. Polstein, M. Juhas, G. Hanna, N. Bursac and C. A. Gersbach, *ACS Synth. Biol.*, 2017, **6**, 2003–2013.
17 J. Li, Y. Hao, H. Pan, Y. Zhang, G. Cheng, B. Liu, J. Chang and H. Wang, *ACS Appl. Bio Mater*, 2021, **4**, 2502–2513.
18 H. K. Kim, A. L. Alexander and I. Soltesz, in *Optogenetics: A Roadmap*, ed. A. Stroh, Springer, New York, NY, 2018, pp. 277–300.
19 R. Winter, P. Dungel, F. M. J. Reischies, S. Rohringer, P. Slezak, C. Smolle, S. Spendel, L.-P. Kamolz, N. Ghaffari-Tabrizi-Wizsy and K. Schicho, *Sci. Rep.*, 2018, **8**, 17080.
20 S.-W. Kim, Y.-J. Kim, G.-B. Im, Y. H. Kim, G.-J. Jeong, S. M. Cho, H. Lee and S. H. Bhang, *Cell Biol. Toxicol.*, 2021, **39**, 217–236.
21 Y. Li, Q. Xu, M. Shi, P. Gan, Q. Huang, A. Wang, G. Tan, Y. Fang and H. Liao, *Microvasc. Res.*, 2020, **129**, 103959.
22 S. Rohringer, W. Holnthoner, S. Chaudary, P. Slezak, E. Priglinger, M. Strassl, K. Pill, S. Mühleder, H. Redl and P. Dungel, *Sci. Rep.*, 2017, **7**, 10700.
23 J. Bai, L. Li, N. Kou, Y. Bai, Y. Zhang, Y. Lu, L. Gao and F. Wang, *Stem Cell Res. Ther.*, 2021, **12**, 432.
24 X. Wang, F. Tian, S. S. Soni, F. Gonzalez-Lima and H. Liu, *Sci. Rep.*, 2016, **6**, 30540.
25 S. Negri, P. Faris, G. Tullii, M. Vismara, A. F. Pellegata, F. Lodola, G. Guidetti, V. Rosti, M. R. Antognazza and F. Moccia, *Cell Calcium*, 2022, **101**, 102502.
26 F. Lodola, V. Rosti, G. Tullii, A. Desii, L. Tapella, P. Catarsi, D. Lim, F. Moccia and M. R. Antognazza, *Sci. Adv.*, 2019, **5**, eaav4620.
27 F. Moccia, S. Negri, P. Faris, C. Ronchi and F. Lodola, *Vasc. Pharmacol.*, 2022, **144**, 106998.
28 V. Benfenati, N. Martino, M. R. Antognazza, A. Pistone, S. Toffanin, S. Ferroni, G. Lanzani and M. Muccini, *Adv. Healthcare Mater.*, 2014, **3**, 392–399.
29 N. Martino, P. Feyen, M. Porro, C. Bossio, E. Zucchetti, D. Ghezzi, F. Benfenati, G. Lanzani and M. R. Antognazza, *Sci. Rep.*, 2015, **5**, 8911.
30 F. Lodola, N. Martino, G. Tullii, G. Lanzani and M. R. Antognazza, *Sci. Rep.*, 2017, **7**, 8477.
31 G. Tullii, A. Desii, C. Bossio, S. Bellani, M. Colombo, N. Martino, M. R. Antognazza and G. Lanzani, *Org. Electron.*, 2017, **46**, 88–98.
32 S. Samanta, A. A. Beharry, O. Sadovski, T. M. McCormick, A. Babalhavaeji, V. Tropepe and G. A. Woolley, *J. Am. Chem. Soc.*, 2013, **135**, 9777–9784.
33 H. Fu, Z. Wang and Y. Sun, *Angew. Chem., Int. Ed.*, 2019, **58**, 4442–4453.
34 Z. Zheng, H. Yao, L. Ye, Y. Xu, S. Zhang and J. Hou, *Mater. Today*, 2020, **35**, 115–130.
35 S. K. Murthy, *Int. J. Nanomed.*, 2007, **2**, 129–141.
36 Y. Wang, L. Feng and S. Wang, *Adv. Funct. Mater.*, 2019, **29**, 1806818.

37 D. J. Medina-Leyte, M. Domínguez-Pérez, I. Mercado, M. T. Villarreal-Molina and L. Jacobo-Albavera, *Appl. Sci.*, 2020, **10**, 938.
38 C. Zhang, V. J. Pansare, R. K. Prud'homme and R. D. Priestley, *Soft Matter*, 2012, **8**, 86–93.
39 W. S. Saad and R. K. Prud'homme, *Nano Today*, 2016, **11**, 212–227.
40 G. Carpentier, S. Berndt, S. Ferratge, W. Rasband, M. Cuendet, G. Uzan and P. Albanese, *Sci. Rep.*, 2020, **10**, 11568.
41 A. Holmes, E. Deniau, C. Lartigau-Dagron, A. Bousquet, S. Chambon and N. P. Holmes, *ACS Nano*, 2021, **15**, 3927–3959.
42 A. Pitto-Barry and N. P. E. Barry, *Polym. Chem.*, 2014, **5**, 3291–3297.
43 A. V. Kabanov, E. V. Batrakova and V. Y. Alakhov, *J. Controlled Release*, 2002, **82**, 189–212.
44 H. Mohan, M. Bartkowski and S. Giordani, *Appl. Sci.*, 2021, **11**, 10565.
45 C. Kim, S.-Y. Kim, Y. T. Lim and T. S. Lee, *Macromol. Res.*, 2017, **25**, 572–577.
46 M. Zhao, E. Leggett, S. Bourke, S. Poursanidou, S. Carter-Searjeant, S. Po, M. Palma do Carmo, L. A. Dailey, P. Manning, S. G. Ryan, L. Urbano, M. A. Green and A. Rakovich, *ACS Nano*, 2021, **15**, 8790–8802.
47 G. Nagarjuna, M. Baghgar, J. A. Labastide, D. D. Algaier, M. D. Barnes and D. Venkataraman, *ACS Nano*, 2012, **6**, 10750–10758.
48 M.-C. Wu, Y.-Y. Lin, S. Chen, H.-C. Liao, Y.-J. Wu, C.-W. Chen, Y.-F. Chen and W.-F. Su, *Chem. Phys. Lett.*, 2009, **468**, 64–68.
49 F. Bencheikh, D. Duché, C. M. Ruiz, J.-J. Simon and L. Escoubas, *J. Phys. Chem. C*, 2015, **119**, 24643–24648.
50 S. Seo, J. Kim, H. Kang, J.-W. Lee, S. Lee, G.-U. Kim and B. J. Kim, *Macromolecules*, 2021, **54**, 53–63.
51 E. Gutiérrez-Fernández, T. A. Ezquerra, E. Rebollar, J. Cui, S. Marina, J. Martín and A. Nogales, *Polymer*, 2021, **218**, 123515.
52 C. Bossio, I. Abdel Aziz, G. Tullii, E. Zucchetti, D. Debellis, M. Zangoli, F. Di Maria, G. Lanzani and M. R. Antognazza, *Front. Bioeng. Biotechnol.*, 2018, **6**, 114.
53 J. Rhim, *Carcinogenesis*, 1998, **19**, 673–681.
54 B. A. Saeed, V. Lim, N. A. Yusof, K. Z. Khor, H. S. Rahman and N. Abdul Samad, *Int. J. Nanomed.*, 2019, **14**, 5135–5146.
55 R. Augustine, A. P. Mathew and A. Sosnik, *Appl. Mater. Today*, 2017, **7**, 91–103.
56 S. Negri, P. Faris and F. Moccia, *Int. J. Mol. Sci.*, 2021, **22**, 9821.
57 H. Sies and D. P. Jones, *Nat. Rev. Mol. Cell Biol.*, 2020, **21**, 363–383.
58 P. P. Fu, Q. Xia, H.-M. Hwang, P. C. Ray and H. Yu, *J. Food Drug Anal.*, 2014, **22**, 64–75.
59 J. L. Martindale and N. J. Holbrook, *J. Cell. Physiol.*, 2002, **192**, 1–15.
60 D. Trachootham, J. Alexandre and P. Huang, *Nat. Rev. Drug Discovery*, 2009, **8**, 579–591.
61 S. J. Glassman, *Clin. Sci.*, 2010, **120**, 99–120.
62 W. Dröge, *Physiol. Rev.*, 2002, **82**, 47–95.
63 P. Newsholme, P. I. Homem De Bittencourt Jr., C. O' Hagan, G. De Vito, C. Murphy and M. S. Krause, *Clin. Sci.*, 2009, **118**, 341–349.
64 M. Y. Lee and K. K. Griendling, *Antioxid. Redox Signaling*, 2008, **10**, 1045–1059.
65 G. Saravanakumar, J. Kim and W. J. Kim, *Adv. Sci.*, 2017, **4**, 1600124.
66 H. Wang and J. A. Joseph, *Free Radicals Biol. Med.*, 1999, **27**, 612–616.
67 C. C. Chua, R. C. Hamdy and B. H. L. Chua, *Free Radical Biol. Med.*, 1998, **25**, 891–897.
68 M. Ushiofukai, *Cardiovasc. Res.*, 2006, **71**, 226–235.
69 M. Malferrari, G. Tullii, C. Ronchi, C. Marzuoli, I. A. Aziz, M. R. Antognazza and S. Rapino, *Electrochim. Acta*, 2023, 142429.
70 M. I. Setyawati and D. T. Leong, *ACS Appl. Mater. Interfaces*, 2017, **9**, 6690–6703.
71 K.-J. Oh, J. Park, H.-S. Lee and K. Park, *Int. J. Impotence Res.*, 2018, **30**, 312–317.
72 S. M. L. Terena, R. A. Mesquita-Ferrari, A. M. de Siqueira Araújo, K. P. S. Fernandes and M. H. Fernandes, *Lasers Med. Sci.*, 2021, **36**, 83–90.
73 J. Yao, B. Liu and F. Qin, *Biophys. J.*, 2009, **96**, 3611.